

Observing Dynamical Phases of a Bardeen-Cooper-Schrieffer Superconductor in a Cavity QED Simulator

Dylan J. Young,^{1,*} Anjun Chu,^{1,2,*} Eric Yilun Song,¹ Diego Barberena,^{1,2} David Wellnitz,^{1,2} Zhijing Niu,¹ Vera M. Schäfer,^{1,3} Robert J. Lewis-Swan,^{4,5} Ana Maria Rey,^{1,2} and James K. Thompson¹

¹*JILA, NIST, and Department of Physics, University of Colorado, Boulder, CO, USA*

²*Center for Theory of Quantum Matter, University of Colorado, Boulder, CO, USA*

³*Max-Planck-Institut für Kernphysik, Saupfercheckweg 1, 69117 Heidelberg, Germany*

⁴*Homer L. Dodge Department of Physics and Astronomy, University of Oklahoma, Norman, OK, USA*

⁵*Center for Quantum Research and Technology, University of Oklahoma, Norman, OK, USA*

(Dated: May 31, 2023)

In conventional Bardeen-Cooper-Schrieffer (BCS) superconductors [1], electrons with opposite momenta bind into Cooper pairs due to an attractive interaction mediated by phonons in the material. While superconductivity naturally emerges at thermal equilibrium, it can also emerge out of equilibrium when the system’s parameters are abruptly changed [2–8]. The resulting out-of-equilibrium phases are predicted to occur in real materials and ultracold fermionic atoms but have not yet been directly observed. This work realizes an alternate way to generate the proposed dynamical phases using cavity quantum electrodynamics (cavity QED). Our system encodes the presence or absence of a Cooper pair in a long-lived electronic transition in ⁸⁸Sr atoms coupled to an optical cavity and represents interactions between electrons as photon-mediated interactions through the cavity [9]. To fully explore the phase diagram, we manipulate the ratio between the single-particle dispersion and the interactions after a quench and perform real-time tracking of subsequent dynamics of the superconducting order parameter using non-destructive measurements. We observe regimes where the order parameter decays to zero (“phase I”) [2, 4], assumes a non-equilibrium steady-state value (“phase II”) [3], or exhibits persistent oscillations (“phase III”) in the form of a self-generated Floquet phase [2]. The capability to emulate these dynamical phases in optical cavities without real Cooper pairs demonstrates that programmable simulators can overcome many challenges faced by traditional approaches. This opens up exciting prospects for quantum simulation, including the potential to engineer unconventional superconductors and to probe beyond mean-field effects like the spectral form factor [10, 11], and for increasing coherence time for quantum sensing.

INTRODUCTION

Analog quantum simulators mimic the evolution of other quantum systems and offer the promise to solve open problems in many-body physics that cannot be meaningfully modeled or controllably realized in natural settings. Quantum simulation offers a path to understand a broad range of phenomena, from high-temperature superconductivity and correlated quantum magnetism in condensed matter physics [12] to quarks and gluons in nuclei and matter under extreme conditions [13], as well as the black hole information paradox in gravitational physics [14].

A fascinating and promising case is the prethermal dynamical phases [15] predicted to emerge from quenches of superconductors and superfluids [2, 6, 16–21], systems that feature Cooper pairing of electrons or neutral fermions. While there has been great progress in pump-probe experiments of superconductors to induce such fast quenches using THz technology [3, 16, 22, 23], the intense pulses couple nonlinearly to the Cooper pairs in the superconductor, thus complicating a clean observation of the dynamical phases. For these reasons, the realization of fermionic superfluids in ultracold atomic

gases [24] has generated great excitement [2–8]. However, a major challenge so far has been the requirement to achieve the necessary ultracold temperatures at which the relevant BCS dynamics manifests, and to date none of the nontrivial predicted dynamical phases have been observed in fermionic superfluids.

Here, we take a step forward towards this challenge by circumventing the need to reach ultracold motional temperatures, using internal electronic states—which can be cooled down to extremely low effective temperatures—to encode effective Cooper pairs. At the heart of this implementation is the Anderson pseudospin mapping [25] by which the presence or absence of Cooper pairs in a momentum mode is encoded in a pseudo spin-1/2 system. We simulate Anderson pseudospins using a long-lived electronic transition in ⁸⁸Sr with interactions between the spins mediated by a high finesse optical cavity. As proposed in Ref. [9], the interactions between electrons in condensed matter systems, which are mediated by phonons in the crystal, can be engineered in our system via the exchange of photons through the cavity (see Fig. 1d). In this way, the low-energy physics of a superconductor or superfluid can be mapped onto the dynamics of a collection of interacting spin-1/2 systems.

For the first time, we probe all three dynamical phases (phases I, II, and III) predicted to exist in BCS superconductors by taking advantage of the high degree

* These authors contributed equally to this work.

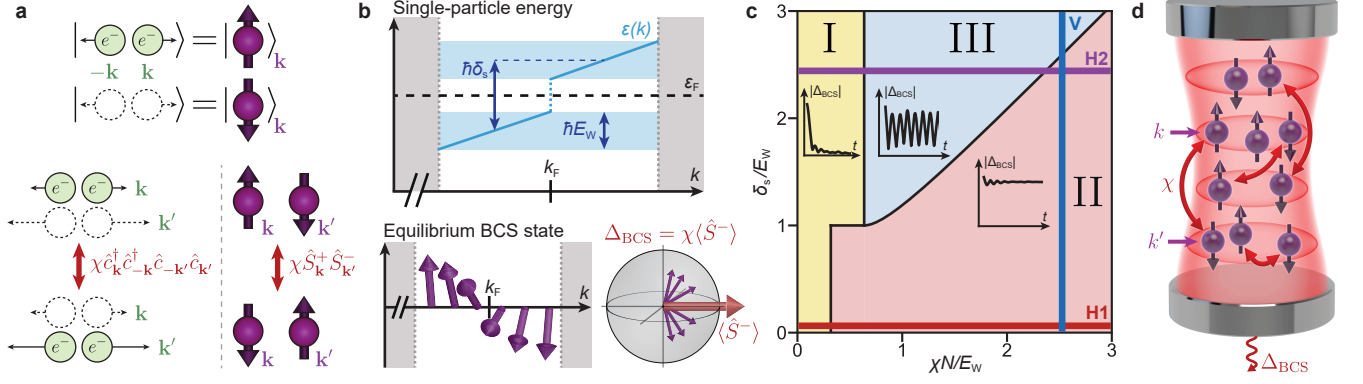


Fig. 1. Engineering BCS dynamical phases. **a**, The Anderson pseudospin mapping encodes the presence and absence of a Cooper pair into the up and down states of a spin-1/2 system, respectively. Under this mapping, the phonon-mediated attraction between electrons, which to leading order causes an exchange interaction $\chi \hat{c}_{\mathbf{k}}^\dagger \hat{c}_{-\mathbf{k}}^\dagger \hat{c}_{-\mathbf{k}'} \hat{c}_{\mathbf{k}'}$ between Cooper pairs with momenta \mathbf{k} and \mathbf{k}' , gives rise to an all-to-all exchange interaction $\chi \hat{S}_{\mathbf{k}}^+ \hat{S}_{\mathbf{k}'}^-$ between pseudospins. **b**, Model parameters. The top plot shows the effective dispersion relation near the Fermi surface engineered in our system as a function of parameters δ_s and E_W , controlled using AC Stark shifts. The bottom plot visualizes the ground state of a BCS superconductor using Anderson pseudospins: low-energy states are all occupied and thus map to spin-up, whereas high-energy states are empty and point down. Near the Fermi momentum, the pseudospins develop a phase-coherent superposition at a scale set by a nonzero BCS pairing gap Δ_{BCS} . This gap is self-consistently defined from the spin coherence as shown on the Bloch sphere. **c**, Dynamical phase diagram. The three dynamical phases can be realized by varying parameters χN , δ_s , and E_W . Representative dynamics of $|\Delta_{\text{BCS}}|$ for each phase are shown as insets. We explore cuts H1, V, and H2 in Figs. 2, 3, and 4 respectively. **d**, Cavity-QED implementation of the BCS interaction. Coupling a long-lived transition in strontium atoms to a detuned optical cavity generates infinite-range spin-exchange interactions mediated by a virtual exchange of cavity photons. This interaction also causes a field proportional to the BCS order parameter Δ_{BCS} to leak out of the cavity, providing a real-time probe of the dynamics.

of control and flexibility in state initialization, interaction control, and non-destructive measurements provided by the coupling of long-lived atoms to an optical cavity. Behaviors intrinsic to “phase I” (normal phase) and “phase II” (finite steady-state superconductivity) have previously been observed in cavity systems [26, 27], and in two-level fermionic [28], bosonic [29, 30], and thermal atoms [31] interacting via collisions. We build on this work by clarifying the connection between these dynamical phases from the BCS model and the physics of many-body gap protection in spin systems. Notably, our results also provide the first demonstration of “phase III” (a self-generated Floquet phase, featuring persistent superconducting oscillations), which is predicted to dynamically emerge in superconductors via quenches from weak to strong interactions [5]. In our system, we instead engineer this phase using flexible control of the single-particle dispersion, dynamically resembling the low-energy condition of a BCS superconductor. For all experiments, we perform real-time tracking of the superconducting order parameter, enabling fast readout of the dynamics.

EXPERIMENTAL SETUP AND MODEL SYSTEM

To realize dynamical phases of the BCS model, we laser cool an ensemble of $N = 10^5 - 10^6$ ^{88}Sr atoms and trap them inside a $\lambda_L = 813$ nm 1D optical lattice supported by a high-finesse optical cavity. A spin-

1/2 system is encoded in the electronic ground state $|\downarrow\rangle = |^1S_0, m_J = 0\rangle$ and a long-lived optical excited state $|\uparrow\rangle = |^3P_1, m_J = 0\rangle$ with transition frequency ω_a . Along this transition, we define spin operators $\hat{S}_k^- = |\downarrow\rangle\langle\uparrow|_k$ and $\hat{S}_k^z = (|\uparrow\rangle\langle\uparrow|_k - |\downarrow\rangle\langle\downarrow|_k)/2$ for single atoms with labels $k \in \{1, \dots, N\}$, as well as the collective lowering operator $\hat{S}^- = \sum_k \hat{S}_k^-$ and raising operator $\hat{S}^+ = (\hat{S}^-)^\dagger$.

In this system, we engineer an effective Hamiltonian of the form

$$\hat{H}/\hbar = \chi \hat{S}^+ \hat{S}^- + \sum_k \epsilon_k \hat{S}_k^z. \quad (1)$$

The first term represents an infinite-range spin-exchange interaction, realized using the collective coupling between the atomic ensemble and a detuned optical cavity mode with resonance frequency ω_c (see Methods for modifications due to inhomogeneity in the atom-light coupling). The interaction strength is characterized by $\chi = -g^2/\delta_c$, where $2g$ is the single-photon Rabi frequency describing the atom-cavity coupling strength, and $\delta_c = \omega_c - \omega_a$ is the cavity detuning from the atomic transition. Previously, we have characterized this interaction [27] and studied collective dynamics by applying an external drive [32]. In this work, we go beyond the fully collective manifold by engineering a single-particle spread in transition frequencies $\{\epsilon_k\}$ using applied AC Stark shifts. These shifts form the second term in the Hamiltonian and compete with the spin-exchange interaction.

Equation (1) is the so-called Richardson-Gaudin spin

model [33], which describes the low-energy physics of Bardeen-Cooper-Schrieffer (BCS) superfluids and superconductors using the Anderson pseudospin mapping. This mapping relates the presence (or absence) of a Cooper pair formed by a pair of electrons with momentum \mathbf{k} and $-\mathbf{k}$ to a spin-up (or down) at momentum \mathbf{k} , as shown in Fig. 1a. Correspondingly, annihilating a Cooper pair maps to a spin lowering operator by the relation $\hat{S}_{\mathbf{k}}^- := \hat{c}_{\mathbf{k}}\hat{c}_{-\mathbf{k}}$, where $\hat{c}_{\pm\mathbf{k}}$ are fermionic annihilation operators. Similarly, the spin operator $2\hat{S}_{\mathbf{k}}^z + 1 := \hat{c}_{\mathbf{k}}^\dagger\hat{c}_{\mathbf{k}} + \hat{c}_{-\mathbf{k}}^\dagger\hat{c}_{-\mathbf{k}}$ counts the number of electrons in momentum $\pm\mathbf{k}$. Our cavity system therefore manifestly implements a BCS superconductor if one identifies the label k of an atom in the cavity with the momentum \mathbf{k} of the electrons in a Cooper pair. In this way, the first term in Eq. (1) is equivalent to the attractive interaction between Cooper pairs, and the second term can be associated with the kinetic energy of the Cooper pairs.

The BCS order parameter in the Anderson mapping is defined here by $\Delta_{\text{BCS}} = \chi\langle\sum_{\mathbf{k}}\hat{c}_{\mathbf{k}}\hat{c}_{-\mathbf{k}}\rangle = \chi\langle\hat{S}^-\rangle$, as depicted in Fig. 1b. In equilibrium, it plays the role of the BCS pairing gap, which energetically favors many-body states where the electrons arrange in a coherent superposition between Cooper pairs and holes for states close to the Fermi energy. Away from equilibrium, Δ_{BCS} is also predicted to characterize the three dynamical phases that arise after quenches in superconductors and superfluids, which are called phases I, II, and III [15]. Such dynamical phases represent distinct regimes of dynamical behavior that arise after a sudden quench of a control parameter in a closed many-body system. They are described using a time-averaged or steady-state order parameter that demonstrates non-analytic behavior at the boundary between phases.

Phase I is characterized by a steady state with a vanishing order parameter $|\Delta_{\text{BCS}}(t)| \rightarrow 0$ at long times after the quench. Phase II exhibits a steady state with a constant nonzero order parameter $|\Delta_{\text{BCS}}(t)| \rightarrow \Delta_\infty > 0$. Finally, phase III features oscillations in $|\Delta_{\text{BCS}}(t)|$ that persist to long times and therefore realizes a Floquet superfluid, despite not being periodically driven [5–7, 34]. The long-time behavior of these dynamical phases admits a simpler description in terms of the Lax-reduced Hamiltonian, which is an effective Hamiltonian taking the same form of Eq. (1) but with rescaled parameters and a reduced number of spins [6]. Under this formulation, phases I, II, and III emerge when the Lax-reduced Hamiltonian describes effective zero-spin, one-spin, and two-spin systems respectively.

Inspired by the Lax-reduced Hamiltonian, we engineer a single-particle dispersion $\epsilon(k)$ with an overall splitting $\hbar\delta_s$ between two different sub-ensembles of atoms and an energy width $\hbar E_W$ of each sub-ensemble (see Fig. 1b). To perform quenches, we initialize all the atoms in the $|\downarrow\rangle$ state and then apply a coherent $\pi/2$ pulse through the cavity in 100 ns such that $\Omega \gg \chi N$, where Ω is the pulse Rabi frequency and χN is the characteristic interaction strength for an ensemble of N atoms. This establishes a

large BCS order parameter Δ_{BCS} on a timescale faster than any other relevant dynamics. The prepared state mimics the ground state of a Hamiltonian with an infinite interaction strength χ . We then quench the system by rapidly turning on the single-particle dispersion $\epsilon(k)$, which sets a finite ratio $\chi N/E_W$ and allows us to explore the dynamical phase diagram shown in Fig. 1c.

We measure both the pre and post-quench dynamics of $|\Delta_{\text{BCS}}|$ by monitoring light emitted by the atoms into the cavity as a function of time (see Fig. 1d). This light arises from a superradiance process which is suppressed by the large cavity detuning $|\delta_c| \gg \kappa$ [35–37]. In this limit, the established cavity field adiabatically follows $\langle\hat{S}^-\rangle$, which is proportional to the pairing gap Δ_{BCS} . By measuring the leakage of light from the cavity in heterodyne with a local oscillator, we therefore obtain a real-time probe of Δ_{BCS} . Importantly, at the chosen detuning δ_c this probe is quasi-nondestructive, since only a small fraction of the atoms emit light over relevant timescales. In plots of $|\Delta_{\text{BCS}}|$ over time, we normalize traces to the initial gap size Δ_{init} measured right after the $\pi/2$ pulse.

PHASE I TO PHASE II

We probe the phase I to phase II transition by varying the ratio $\chi N/E_W$ between the interaction strength and the width of the single-particle energy distribution. As shown in Fig. 2a, we shine an off-resonant 461 nm beam onto the atomic cloud from the side of the cavity that generates a distribution of AC Stark shifts with a spread in energies $\hbar E_W$. We calculate the engineered single-particle dispersion by labeling our atoms in order of increasing single-particle energy and plot this energy ϵ as a function of label k . Careful shaping of the 461 nm beam allows us to realize a roughly linear dispersion (see Methods), mimicking real superconductors whose dispersion can usually be linearized about the Fermi energy. As mentioned above, we initialize a highly coherent initial state with a $\pi/2$ pulse, placing the system far into phase II. After waiting for 2 μs to let transient dynamics settle, we then turn on the 461 nm beam to quench on $E_W/2\pi = 0.83$ MHz from an initial value $E_W^{(0)}/2\pi \ll 0.1$ MHz. The beam exhibits a rise time of roughly 50 ns, much faster than the relevant dynamics. To scan across the phase diagram (see the inset of Fig. 2b), we vary the interaction strength χN between shots by changing the atom number N .

As shown in Fig. 2b, we observe two distinct dynamical behaviors corresponding to phases I and II, signaled by the decay rate of $|\Delta_{\text{BCS}}|$. For experiments with sufficiently small χN , such as $\chi N/2\pi = 0.19$ MHz, $|\Delta_{\text{BCS}}|$ decays with a $1/e$ coherence time of 0.9 ± 0.1 μs . This coherence time is consistent with single-particle dephasing of $\langle\hat{S}^-\rangle$ set by the energy spread $\hbar E_W$ and is nearly constant throughout this regime. We identify the fast decay of $|\Delta_{\text{BCS}}|$ as an experimental signature of phase I. For larger interaction strengths, we observe a rapid increase

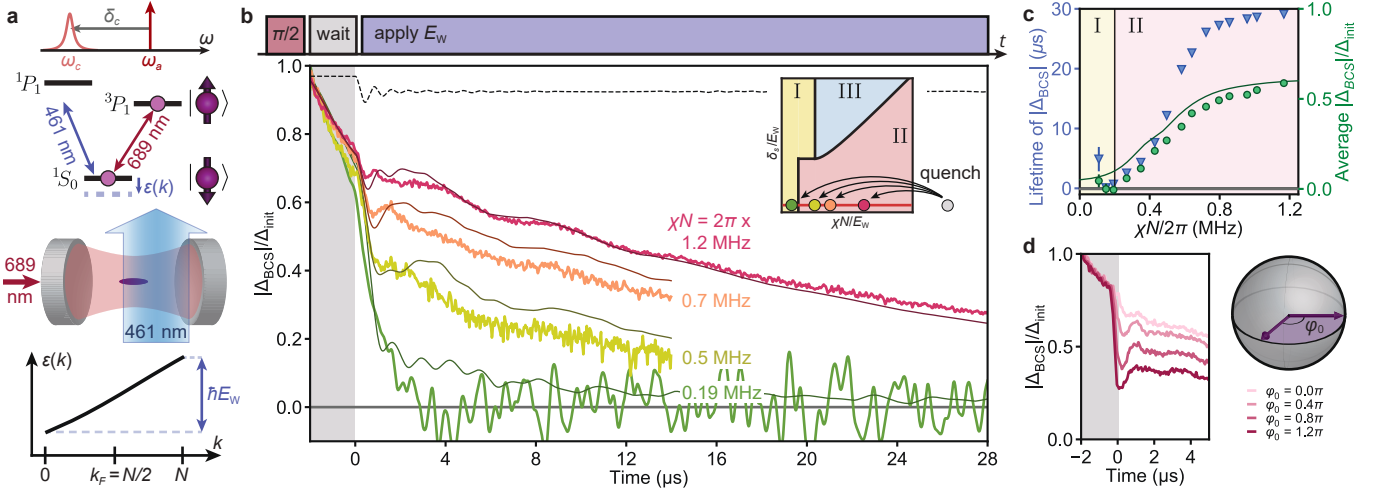


Fig. 2. Phase I to phase II transition. **a**, Tuning the single particle dispersion. We shine an off-resonant 461 nm beam onto the cloud of atoms from the side of the cavity. This generates a distribution of AC Stark shifts with an equivalent dispersion relation that is roughly linear, as shown in the bottom plot. **b**, Probing phase I to phase II dynamics using time traces of $|\Delta_{\text{BCS}}|$. As shown in the timing sequence at the top, we perform a rapid $\pi/2$ pulse to prepare a highly coherent initial state corresponding to a large gap ($\chi N/E_W \gg 1$), wait for 2 μs , and then quench to a finite $\chi N/E_W$ with $\delta_s = 0$ and let the system evolve. The inset shows the explored cut through the phase diagram and identifies the final $\chi N/E_W$ values with colored dots. The main plot shows numerical simulations (solid dark lines) corresponding to experimental traces (colored curves). Two such curves are extended to 28 μs to demonstrate coherence protection at long times. The $\chi N/2\pi = 0.19$ MHz trace is smoothed for clarity. For $\chi N/2\pi = 1.2$ MHz, we simulate an ideal time trace neglecting dissipation and axial motion effects (dashed line—see Methods for a discussion of axial effects), which exhibits transient “Higgs” oscillations but with a faster damping rate. Experimental data also shows similar oscillations but with a faster damping rate. **c**, Characterizing the phase transition. Blue triangles show the fitted coherence time of $|\Delta_{\text{BCS}}(t)$ from $t = 1$ μs to 30 μs . Green circles show the time-averaged gap size in a bin from $t = 3$ μs to 8 μs vs. interaction strength, with the dark green line representing numerical simulations. In all cases, we identify a phase transition at $\chi N/2\pi = 0.2$ MHz. Error bars in all plots are calculated using jackknife resampling on shots of the experiment. **d**, Varying initial conditions. To reduce the pre-quench value of $|\Delta_{\text{BCS}}|$, we apply light pulses to produce a differential phase spread φ_0 as shown on the Bloch sphere. Traces represent data taken in phase II for different initial dephasing pulses, which show an increase in the Higgs oscillation amplitude with increasing φ_0 .

in coherence time up to 29 μs when $\chi N/2\pi = 1.2$ MHz as shown in Fig. 2c; this constitutes an improvement of more than a factor of 30. We identify this large χN regime as phase II. The residual decay of $|\Delta_{\text{BCS}}|$ in this regime can be primarily attributed to intrinsic dissipative processes including spontaneous emission and off-resonant superradiant emission as described in the previous section [27, 37], which set a maximum coherence time of 31 μs (see Methods). All experimental observations (colored traces) are in good agreement with numerical simulations based on experimental conditions (dark lines—see Methods).

The separation of timescales in the decay of $|\Delta_{\text{BCS}}|$ allows us to determine the boundary between phase I and phase II in our experiment. We calculate the average $|\Delta_{\text{BCS}}|$ in a time window from 3 μs to 8 μs as a function of χN , as shown in Fig. 2c. In this analysis, phase I features a vanishing average $|\Delta_{\text{BCS}}|$, while phase II sees a nonzero $|\Delta_{\text{BCS}}|$ that increases with χN . The sharp rise of average $|\Delta_{\text{BCS}}|$ around $\chi N/2\pi = 0.2$ MHz indicates a dynamical phase transition, which agrees with the location predicted by numerical simulations.

Additionally, the observation of an enhanced coherence time shows that phase II physics can be understood

in the context of many-body gap protection [38]. In a spin-model picture, the BCS pairing gap corresponds to the energy gap between collective angular momentum states, which exists due to the spin-exchange interaction $\chi \hat{S}^+ \hat{S}^-$. Phase II corresponds to the parameter region where such interactions are sufficiently strong to protect against single-particle dephasing. As a result, the observed transition directly relates to previous experiments exploring coherence protection in other systems [26–31].

In BCS superconductors, the excitation of a Higgs mode is predicted to occur in phase II. This mode can be characterized by a collective damped oscillation of the order parameter $|\Delta_{\text{BCS}}|$ with a characteristic frequency of $2\Delta_\infty$ [6]. We observe hints of Higgs oscillations by comparing the experimental trace of $|\Delta_{\text{BCS}}|$ at $\chi N/2\pi = 1.2$ MHz (red curve in Fig. 2b) with the dissipation-free simulation (dashed line in Fig. 2b), where the first dip in the experimental trace coincides with the first cycle of Higgs oscillations. The amplitude of Higgs oscillations can be increased experimentally by engineering an initial phase spread φ_0 , as shown in Fig. 2d. The initial state with a nonzero opening angle φ_0 shares qualitative features with the BCS ground state at finite χ up to a $\pi/2$ rotation on the Bloch sphere [9], in contrast to the ini-

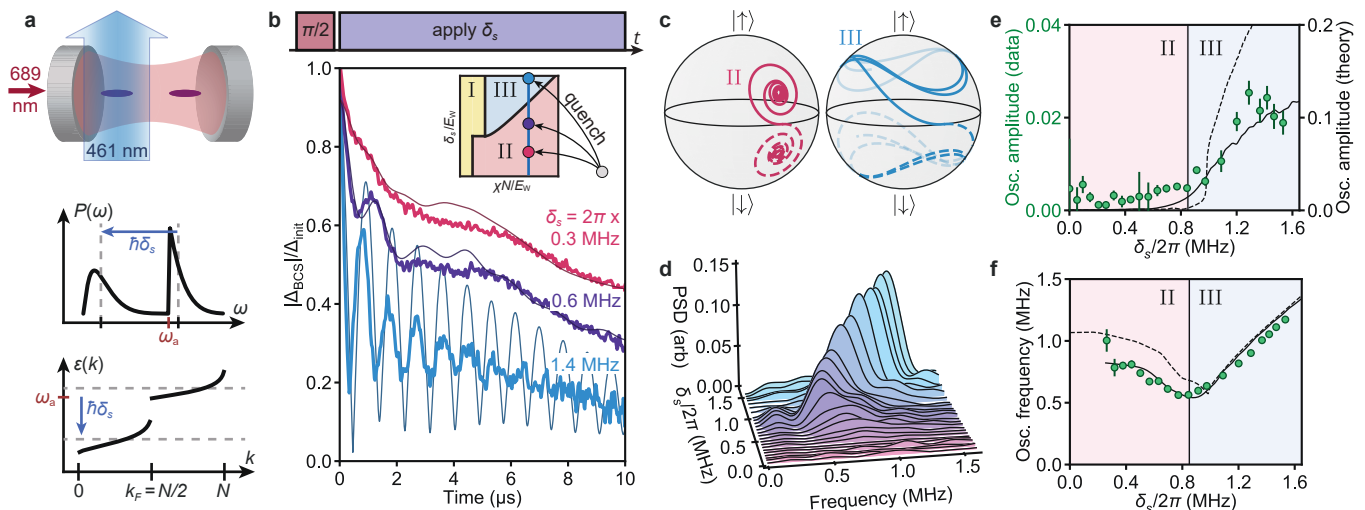


Fig. 3. Phase II to phase III transition. **a**, Engineering a bimodal energy distribution. We split our atomic ensemble into clouds with centers separated by 3 mm and shine an off-resonant 461 nm beam centered on one of them. This generates a distribution of transition frequencies as shown in the middle plot, equivalent to a dispersion relation as shown on the bottom. We define a splitting $\hbar\delta_s$ as the difference in average energies between the two ensembles. **b**, Probing phase II to phase III dynamics using time traces of $|\Delta_{\text{BCS}}|$. As shown in the timing sequence at the top, we prepare the same initial state as in Fig. 2b with a $\pi/2$ pulse, quench to a finite δ_s/E_W , and then let the system evolve. The inset shows the explored cut through the phase diagram and identifies the final δ_s/E_W values with colored dots. As before, colored traces represent experimental data, and solid dark lines correspond to numerical simulations with the same system parameters. **c**, Ideal simulations of the mean-field Bloch vector trajectories of the two sub-ensembles, shown as solid and dashed curves respectively, in phase II (magenta) and phase III (blue). The trajectories are projected onto the surface of the Bloch sphere for visual clarity. In phase II, the sub-ensembles exhibit phase-locking behavior, while in phase III they accrue an unbounded azimuthal phase over time. **d**, Fourier response of dynamics with slow-moving behavior subtracted for clarity. We show power spectral densities of the dynamics of the squared BCS gap on a timescale from $t = 0.5 \mu\text{s}$ to $4 \mu\text{s}$. Different curves correspond to different δ_s . **e**, Average oscillation amplitude between $t = 3 \mu\text{s}$ and $8 \mu\text{s}$, with a smaller y scale for the experimental data (left axis) compared with numerical simulations (right axis). For the remaining plots, dashed lines represent an ideal model without dissipation or axial motion effects, and solid dark lines correspond to a full simulation. We identify the phase transition around $\delta_s = 2\pi \times 0.85$ MHz. **f**, Oscillation frequency of gap dynamics vs. applied splitting, measured using power spectral densities calculated in (d). The position of the phase transition predicted by the data in panels (e) and (f) agrees well with simulations.

tial state mimicking the BCS ground state with infinite χ in Fig. 2b. In a spin-model picture, increasing φ_0 decreases the pre-quench many-body gap, thus enhancing the excitation of the Higgs mode.

PHASE II TO PHASE III

We probe the phase II to phase III transition using a vertical cut through the dynamical phase diagram. To realize this, we introduce an energy splitting $\hbar\delta_s$ between two individually addressable clouds of atoms along the cavity axis using AC Stark shifts from our 461 nm beam, as shown in Fig. 3a. In combination with a background energy spread $\hbar E_W$ associated with lattice shifts (see Methods), this produces a bimodal distribution of transition frequencies and a dispersion relation similar to the one proposed in Fig. 1b. As before, we begin the experiment with a highly coherent state and with $\delta_s = 0$. Then, we quench on a finite δ_s and let the system evolve. Between shots, we scan δ_s while fixing $\chi N/2\pi = 0.9$ MHz and $E_W/2\pi \approx 0.34$ MHz to explore the vertical cut.

The resulting dynamics show a marked change in the dynamical evolution of $|\Delta_{\text{BCS}}|$ over the scan as shown in Fig. 3b, which we attribute to a transition between phase II and phase III dynamics. For small δ_s , we either see Higgs oscillations which are damped after $3 \mu\text{s}$ (the trace where $\delta_s/2\pi = 0.6$ MHz) or, for very small splittings, no oscillations resolvable above the noise floor ($\delta_s/2\pi = 0.3$ MHz). We associate this regime with phase II since it overlaps with the previously observed phase II dynamics in parameter space. For larger δ_s , curves instead show large-amplitude oscillations that persist for more than $5 \mu\text{s}$ ($\delta_s/2\pi = 1.4$ MHz). We identify the long-lived oscillations in this parameter regime as an experimental signature of phase III.

Intuitively, we can understand the difference between the two phases by identifying the two sub-ensembles of atoms with two Bloch vectors, as shown in Fig. 3c. In phase II, a finite δ_s causes the Bloch vectors to precess in different directions, but the dominant scale χN locks them together to form the solid and dashed magenta orbits. In the presence of inhomogeneities, the orbits decay, but the Bloch vectors maintain phase coherence. On the

other hand, in phase III δ_s is large enough that the two Bloch vectors accrue an unbounded relative phase, as in the blue orbits. The presence of interactions spin-locks each sub-ensemble separately against a finite E_W , leading to persistent oscillations. We emphasize that the effective beating of two large spins in a macroscopic array of spin-1/2 particles is a genuine interaction-driven effect since interactions must be strong enough to lock the spins within each of the sub-ensembles but not strong enough to lock both sub-ensembles together. In our implementation of phase III, the bimodal distribution allows us to dynamically separate the two sub-ensembles, instead of starting with an already split distribution like in weakly interacting BCS ground states featuring a sharp Fermi edge. Despite their qualitative differences, these two situations can be dynamically connected (see Methods).

Similarly to the previous section, we can experimentally define a boundary between phase II and phase III using the separation of timescales observed for oscillations in $|\Delta_{\text{BCS}}|$. Fig. 3e shows the average oscillation amplitude in a time window from $t = 3 \mu\text{s}$ to $8 \mu\text{s}$. In this analysis, we observe a sharp rise in oscillation amplitude at $\delta_s/2\pi = 0.85 \text{ MHz} \approx \chi N/2\pi$ as we increase δ_s , which we identify as a dynamical phase transition. Numerical simulations plotted in Fig. 3e agree fairly well with data in capturing trend behavior and estimating the phase transition point. However, we see a discrepancy in the absolute size of the observed and predicted oscillation amplitudes. We attribute this to an extra dephasing mechanism in our system, likely residual motional effects not captured by the theory model.

In light of this discrepancy, we verify the location of the phase II to phase III transition using the short-time oscillation frequency (from $t = 0.5 \mu\text{s}$ to $4 \mu\text{s}$) as an additional experimental signature. As can be seen in the Fourier responses in Fig. 3d and quantified in Fig. 3f, the oscillation frequency exhibits a dip vs. δ_s at the previously-identified phase boundary. This dip is present in roughly the same location for experiment and theory and is expected to coincide with the phase II to phase III transition (see Supplemental Online Material).

SCAN ACROSS THREE DYNAMICAL PHASES

Further understanding of the dynamical phase diagram can be achieved by observing all three dynamical phases of the BCS model in a single cut through parameter space, as shown in Fig. 4a. We run the same experimental sequence described in Fig. 3, but instead scan χN between shots with $\delta_s/2\pi = 1.1 \text{ MHz}$ and $E_W/2\pi = 0.46 \text{ MHz}$ fixed. This allows us to probe phase I, phase III and then phase II by increasing atom number N . Using order parameters established in Figs. 2 and 3, we determine boundaries between the three phases. As shown in Fig. 4b, the long-time average of $|\Delta_{\text{BCS}}|$ rises suddenly around $\chi N/2\pi = 0.25 \text{ MHz}$ in both data and simulations. This transition marks the boundary

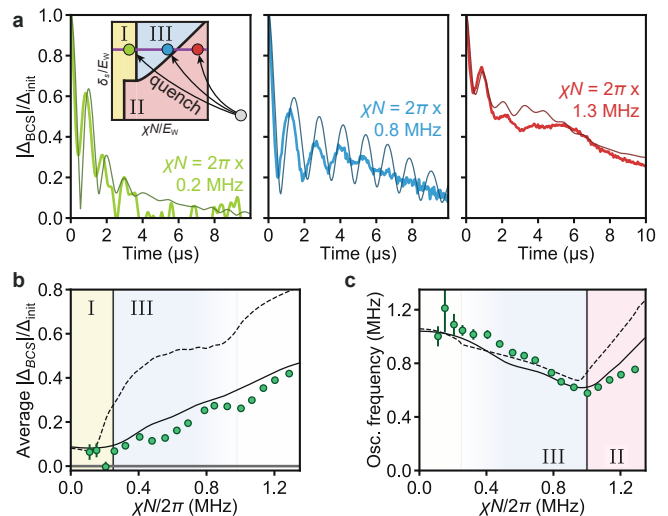


Fig. 4. Scan across three dynamical phases. **a**, Probing phase I, II and III dynamics using time traces of $|\Delta_{\text{BCS}}|$. Quenches are performed in the same manner as in Fig. 3b, except between shots we hold post-quench values of δ_s fixed and vary χN instead. The inset shows the explored cut through the phase diagram and identifies final $\chi N/E_W$ values with green (phase I), blue (phase III), and red (phase II) dots. The $\chi N/2\pi = 0.2 \text{ MHz}$ trace is smoothed for clarity. **b**, Time-averaged gap in a bin from $t = 3 \mu\text{s}$ to $8 \mu\text{s}$ vs. interaction strength. The experimental data shows signatures of a phase I to phase III transition at $\chi N = 2\pi \times 0.25 \text{ MHz}$. **c**, Oscillation frequency of gap dynamics vs. interaction strength in a bin from $t = 0.5 \mu\text{s}$ to $4 \mu\text{s}$. This data identifies a phase III to phase II transition at $\chi N = 2\pi \times 1.0 \text{ MHz}$. Experimental data and transitions in both plots are consistent with numerical simulations.

between phase I, which is characterized by rapid dephasing, and phase III, which exhibits beating between the two sub-ensembles with extended coherence time. Additionally, at $\chi N/2\pi = 1.0 \text{ MHz}$ we observe a dip in the short-time oscillation frequency of $|\Delta_{\text{BCS}}|$ (Fig. 4c), marking a transition between phase III and phase II. For this scan, we do not use the long-time oscillation amplitude as an order parameter due to poor signal-to-noise for smaller values of χN .

CONCLUSION

The demonstrated capability to emulate dynamical phases of superconductors in optical cavities opens exciting prospects for quantum simulation. For example, even though so far we have focused our efforts on simulating conventional superfluids or superconductors, it should be possible to apply an additional optical lattice to upgrade the system and emulate elusive topologically non-trivial superfluid phases such as chiral $p + ip$ [5] and $d_{x^2-y^2} + id_{xy}$ superfluids. So far these exotic systems have not been seen in experiments, but research efforts for studying them have steadily grown in doped

graphene and other novel materials [39–43], as well as in cuprates using magnetic impurities to mix in different pairing channels [44, 45]. It will be fascinating to see if our cavity simulator can, in the near term, engineer and probe these unconventional phases and even understand competing orders of s , p and d superconductivity in a single system, a long standing open question.

Additionally, translating the physics of the BCS dynamical phases into a spin model picture opens up in-

triguing connections to new types of models beyond the scope of standard materials and engineered to exhibit richer and more robust behaviors. For example, by introducing couplings to additional quantum states, we can realize a system where spin-exchange interactions along a two-level manifold provide gap protection against transfer to a third level. Such a system can exhibit similar dynamical phases to the ones present in the standard BCS model and may enable simulation of superfluidity in phenomena relevant to high energy physics [21, 46].

-
- [1] J. Bardeen, L. N. Cooper, and J. R. Schrieffer, *Phys. Rev.* **106**, 162 (1957).
- [2] R. A. Barankov and L. S. Levitov, *Phys. Rev. Lett.* **96**, 230403 (2006).
- [3] E. A. Yuzbashyan, O. Tsypliyatyev, and B. L. Altshuler, *Phys. Rev. Lett.* **96**, 097005 (2006).
- [4] E. A. Yuzbashyan and M. Dzero, *Phys. Rev. Lett.* **96**, 230404 (2006).
- [5] M. S. Foster, M. Dzero, V. Gurarie, and E. A. Yuzbashyan, *Phys. Rev. B* **88**, 104511 (2013).
- [6] E. A. Yuzbashyan, M. Dzero, V. Gurarie, and M. S. Foster, *Phys. Rev. A* **91**, 033628 (2015).
- [7] V. Gurarie, *Phys. Rev. Lett.* **103**, 075301 (2009).
- [8] V. Gurarie and L. Radzihovsky, *Ann. Phys.* **322**, 2 (2007), January Special Issue 2007.
- [9] R. J. Lewis-Swan, D. Barberena, J. R. Cline, D. J. Young, J. K. Thompson, and A. M. Rey, *Phys. Rev. Lett.* **126**, 173601 (2021).
- [10] G. R. Stewart, *Adv. Phys.* **66**, 75 (2017).
- [11] M. Sato and Y. Ando, *Rep. Prog. Phys.* **80**, 076501 (2017).
- [12] X. Zhou, W.-S. Lee, M. Imada, N. Trivedi, P. Phillips, H.-Y. Kee, P. Törmä, and M. Eremets, *Nat. Rev. Phys.* **3**, 462 (2021).
- [13] E. Shuryak, *Rev. Mod. Phys.* **89**, 035001 (2017).
- [14] D. Harlow, *Rev. Mod. Phys.* **88**, 015002 (2016).
- [15] J. Marino, M. Eckstein, M. Foster, and A.-M. Rey, *Rep. Prog. Phys.* **85**, 116001 (2022).
- [16] A. F. Volkov and S. M. Kogan, *JETP* **38**, 1018 (1974), [Russian original - *Zh. Eksp. Teor. Fiz.* **65**, 2038 (1973)].
- [17] R. A. Barankov, L. S. Levitov, and B. Z. Spivak, *Phys. Rev. Lett.* **93**, 160401 (2004).
- [18] E. A. Yuzbashyan, B. L. Altshuler, V. B. Kuznetsov, and V. Z. Enolskii, *Phys. Rev. B* **72**, 220503 (2005).
- [19] E. A. Yuzbashyan, B. L. Altshuler, V. B. Kuznetsov, and V. Z. Enolskii, *J. Phys. A: Math. Gen.* **38**, 7831 (2005).
- [20] E. A. Yuzbashyan, O. Tsypliyatyev, and B. L. Altshuler, *Phys. Rev. Lett.* **96**, 097005 (2006).
- [21] T. Schäfer and D. Teaney, *Rep. Prog. Phys.* **72**, 126001 (2009).
- [22] R. Matsunaga, Y. I. Hamada, K. Makise, Y. Uzawa, H. Terai, Z. Wang, and R. Shimano, *Phys. Rev. Lett.* **111**, 057002 (2013).
- [23] R. Shimano and N. Tsuji, *Annu. Rev. Condens. Matter Phys.* **11**, 103 (2020).
- [24] M. Randeria and E. Taylor, *Annu. Rev. Condens. Matter Phys.* **5**, 209 (2014).
- [25] P. W. Anderson, *Phys. Rev.* **112**, 1900 (1958).
- [26] E. J. Davis, A. Periwal, E. S. Cooper, G. Bentsen, S. J. Evered, K. Van Kirk, and M. H. Schleier-Smith, *Phys. Rev. Lett.* **125**, 060402 (2020).
- [27] M. A. Norcia, R. J. Lewis-Swan, J. R. Cline, B. Zhu, A. M. Rey, and J. K. Thompson, *Science* **361**, 259 (2018).
- [28] S. Smale, P. He, B. A. Olsen, K. G. Jackson, H. Sharum, S. Trotzky, J. Marino, A. M. Rey, and J. H. Thywissen, *Sci. Adv.* **5**, eaax1568 (2019).
- [29] C. Deutsch, F. Ramirez-Martinez, C. Lacroûte, F. Reinhard, T. Schneider, J. N. Fuchs, F. Piéchon, F. Laloë, J. Reichel, and P. Rosenbusch, *Phys. Rev. Lett.* **105**, 020401 (2010).
- [30] A. Kleine, C. Kollath, I. P. McCulloch, T. Giamarchi, and U. Schollwoeck, *New J. Phys.* **10**, 045025 (2008).
- [31] J. C. Allred, R. N. Lyman, T. W. Kornack, and M. V. Romalis, *Phys. Rev. Lett.* **89**, 130801 (2002).
- [32] J. A. Muniz, D. Barberena, R. J. Lewis-Swan, D. J. Young, J. R. Cline, A. M. Rey, and J. K. Thompson, *Nature* **580**, 602 (2020).
- [33] M. Gaudin, *J. Phys. (Paris)* **37**, 1087 (1976).
- [34] M. S. Foster, V. Gurarie, M. Dzero, and E. A. Yuzbashyan, *Phys. Rev. Lett.* **113**, 076403 (2014).
- [35] J. M. Weiner, K. C. Cox, J. G. Bohnet, Z. Chen, and J. K. Thompson, *Appl. Phys. Lett.* **101**, 261107 (2012).
- [36] J. G. Bohnet, Z. Chen, J. M. Weiner, K. C. Cox, and J. K. Thompson, *Phys. Rev. A* **88**, 013826 (2013).
- [37] M. A. Norcia, M. N. Winchester, J. R. Cline, and J. K. Thompson, *Sci. Adv.* **2**, e1601231 (2016).
- [38] A. M. Rey, L. Jiang, M. Fleischhauer, E. Demler, and M. D. Lukin, *Phys. Rev. A* **77**, 052305 (2008).
- [39] A. M. Black-Schaffer, *Phys. Rev. Lett.* **109**, 197001 (2012).
- [40] R. Nandkishore, L. S. Levitov, and A. V. Chubukov, *Nat. Phys.* **8**, 158 (2012).
- [41] M. L. Kiesel, C. Platt, W. Hanke, D. A. Abanin, and R. Thomale, *Phys. Rev. B* **86**, 020507 (2012).
- [42] M. L. Kiesel, C. Platt, W. Hanke, and R. Thomale, *Phys. Rev. Lett.* **111**, 097001 (2013).
- [43] M. H. Fischer, T. Neupert, C. Platt, A. P. Schnyder, W. Hanke, J. Goryo, R. Thomale, and M. Sigrist, *Phys. Rev. B* **89**, 020509 (2014).
- [44] R. Laughlin, *Phys. Rev. Lett.* **80**, 5188 (1998).
- [45] A. V. Balatsky, I. Vekhter, and J.-X. Zhu, *Rev. Mod. Phys.* **78**, 373 (2006).
- [46] Y. Pehlivan, A. Balantekin, T. Kajino, and T. Yoshida, *Phys. Rev. D* **84**, 065008 (2011).
- [47] M. A. Norcia, J. R. Cline, J. A. Muniz, J. M. Robinson, R. B. Hutson, A. Goban, G. E. Marti, J. Ye, and J. K. Thompson, *Phys. Rev. X* **8**, 021036 (2018).
- [48] F. Reiter and A. S. Sørensen, *Phys. Rev. A* **85**, 032111

(2012).

METHODS

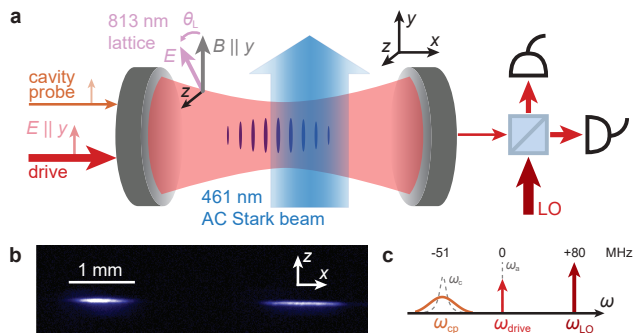
A. Experimental setup: phase I to phase II transition

To explore the phase diagram cut in Fig. 2, we first load $10^5 - 10^6$ ^{88}Sr atoms from a magneto-optical trap into an 813 nm optical lattice supported by a high-finesse optical cavity, similar to previous experiments [27, 32, 37, 47]. The resulting atomic cloud has a temperature of roughly 15 μK , resulting in a Gaussian distribution transverse to the cavity axis with standard deviation $\sigma_y = \sigma_z = 16 \mu\text{m}$ (coordinates defined in Extended Data Fig. 1a). Further, the cloud is extended over thousands of lattice sites, forming a distribution along the cavity axis with a standard deviation $\sigma_x = 430 \mu\text{m}$. We measure an axial trapping frequency of $\omega_x/2\pi = 165 \text{ kHz}$, giving a Lamb-Dicke parameter of $\eta = 0.17$ for excitation with 689 nm light. At the measured temperature, $\eta^2(2\bar{n} + 1) = 0.11 \ll 1$, placing the atoms in the Lamb-Dicke regime. We set a quantization axis along \hat{y} with a 2.4 G magnetic field and tune the lattice polarization to a “magic angle” relative to this axis, such that the differential lattice shift between ground ($|^1S_0\rangle$) and excited ($|^3P_1, m_J = 0\rangle$) states vanishes [32]. Using piezoelectric actuators, we stabilize the cavity length to set the closest TEM₀₀ resonance to be 51 MHz red-detuned from the atomic transition.

After loading into the lattice, we initialize the atoms with a \hat{y} -polarized drive through the cavity which is nominally resonant with the atomic transition. Because the drive is far off-resonance from the cavity (which has linewidth $\kappa/2\pi = 153 \text{ kHz}$ at 689 nm), the induced Rabi frequency is somewhat suppressed. Nonetheless, we find that roughly 5 mW of power before the cavity is sufficient to drive the atoms with a $\pi/2$ pulse in 100 ns. We allow the atoms to settle for 2 μs and then shine a 461 nm beam from the side of the cavity along the \hat{y} direction, detuned from the $|^1S_0\rangle - |^1P_1\rangle$ transition by more than 10 GHz, in order to induce AC Stark shifts on the ground state. The beam has waists $(w_x, w_z) = (1030 \mu\text{m}, 75 \mu\text{m})$ along the \hat{x} and \hat{z} directions at the plane of the atoms, and its center is displaced from the center of the atomic cloud by $x_0 = 580 \mu\text{m}$ along the cavity axis. From these dimensions, we calculate an atomic probability distribution $P(\epsilon)$ as a function of energy shift which is roughly uniform between 0 and a maximum shift $\hbar E_W$.

B. Experimental setup: cuts through phase III

For the two cuts through phase III described in Figs. 3 and 4, we load the atoms in two clouds separated by 3 mm, as shown in Extended Data Fig. 1b. The left cloud has an extent described by standard deviations $(\sigma_x, \sigma_z) = (200 \mu\text{m}, 16 \mu\text{m})$. The right cloud has a similar extent along σ_z but is broader along the cavity axis. We tune the lattice polarization to point along \hat{z} , which



Extended Data Fig. 1. Experimental configuration.

a, Detailed diagram of the cavity and all relevant beams. A magnetic field along \hat{y} sets the quantization axis. The 813 nm optical lattice supported by the cavity has a tunable linear polarization. We drive a $\pi/2$ pulse with a beam polarized along \hat{y} through the cavity, and during the experiment we probe the cavity resonance frequency using a second \hat{y} -polarized beam to measure atom number. A 461 nm beam far-detuned from the $|^1S_0\rangle - |^1P_1\rangle$ transition shines on the atoms from the side of the cavity, inducing AC Stark shifts. We probe signals transmitted through the cavity using a balanced heterodyne detector. **b**, Fluorescence image of the two atomic clouds used when scanning through phase III in Figs. 3 and 4. **c**, Frequency landscape of 689 nm beams. The atomic drive frequency ω_{drive} is resonant with the atomic transition. The cavity probe frequency ω_{cp} is nominally centered with the cavity resonance frequency, 51 MHz red-detuned from the atomic transition. The local oscillator used in heterodyne detection has frequency ω_{LO} and is 80 MHz blue-detuned from the atomic transition.

breaks the magic angle condition and introduces a differential trap depth between ground and excited states of 0.47 MHz for atoms experiencing peak lattice intensity. Due to their finite temperature, the atoms experience a spread in lattice intensities which leads to an inhomogeneous trap depth. We estimate the induced distribution of energy shifts by assuming the atoms occupy a 2D Gaussian distribution radially with standard deviation $\sigma_y = \sigma_z = 16 \mu\text{m}$, compared to the lattice waist $w_y = w_z = 80 \mu\text{m}$. This produces a peaked distribution equivalent to the narrow peak in Fig. 3a.

In these experiments, we perform a $\pi/2$ pulse as before and then immediately shine a 461 nm beam centered on the left (“bright”) atomic cloud. The beam has waists $(w_x, w_z) = (1700 \mu\text{m}, 80 \mu\text{m})$. We install a beam block just before the chamber that clips the beam tail that would otherwise hit the right (“dark”) atomic cloud. The 3 mm separation between clouds is sufficiently large to ensure the beam does not significantly diffract around the beam block. The beam shifts the mean energy of the bright cloud away from that of the dark cloud, introducing a tunable δ_s . While nominally, we hold E_W fixed while scanning δ_s to explore the phase II to phase III transition, in reality the finite size of the blue beam introduces an additional contribution to E_W on the bright cloud. As δ_s increases, therefore, both the size and shape

of the single-particle energy distribution changes. We calculate E_W in a consistent manner by estimating the standard deviation of the bright cloud distribution and matching the result to a uniform distribution with the same standard deviation. In the main text, we report the value of E_W obtained at the phase transition point for the phase II to phase III transition.

C. Readout

After initialization in all experiments, the atomic ensemble establishes a small electric field inside the cavity which adiabatically follows $\langle \hat{S}^- \rangle$ [27]. Assuming homogeneous atom-light coupling (see next section for modifications due to inhomogeneous coupling), this field leaks out of the cavity at a rate

$$\alpha_{\text{out}}(t) = -\frac{g}{\delta_c} \sqrt{\kappa_m} \langle \hat{S}^-(t) \rangle, \quad (2)$$

where α_{out} has units of $\sqrt{\text{photons/s}}$. g and δ_c are as defined in the main text, and κ_m is the rate at which photons incident on the cavity mirror are transmitted. α_{out} is a form of dissipation in the system equivalent to superradiance in a detuned cavity limit. Over the region of parameter space explored in this work, we estimate that the dissipation rate never exceeds $\gamma_{\text{SR}}/2\pi = 2.3$ kHz. Combined with spontaneous emission, this sets a maximum coherence time in the system of 31 μs . We measure the detuned superradiant light as it leaks out of the cavity using balanced heterodyne detection, providing us with a real-time probe of $\langle \hat{S}^- \rangle \propto \Delta_{\text{BCS}}$. In plots of $|\Delta_{\text{BCS}}|$ in the main text, we calculate the square magnitude of this quantity and average over 400-1600 shots of the experiment, taken within 2-10 minutes. We then perform background subtraction to remove vacuum noise power from the heterodyne signal. This subtraction explains why some traces dip below zero.

Additionally, the cavity experiences a (dispersive) shift in its resonance frequency proportional to the number of atoms. We use this fact to measure atom number by sending a pulsed probe tone through the cavity and measuring the frequency shift using the transmitted light. Since this light is spectrally resolved from the light emitted by the atoms, we are able to measure both signals independently on our heterodyne detector. The different optical frequencies involved in the heterodyne beat are compared in Extended Data Fig. 1c.

D. Dynamical phase diagram

The unitary dynamics of our system is modeled by an effective atom-only Hamiltonian,

$$\hat{H} = \hbar\chi \sum_{jk} \zeta_j \zeta_k \hat{S}_j^+ \hat{S}_k^- + \hbar \sum_k \epsilon_k \hat{S}_k^z, \quad (3)$$

where $\chi = -g^2 \delta_c / (\delta_c^2 + \kappa^2/4)$, with $2g$ the single-photon Rabi frequency at an antinode of the cavity mode, κ the cavity linewidth, and $\delta_c = \omega_c - \omega_a$ the cavity detuning from the atomic transition. Here, ω_a is the frequency of the atomic transition, and ω_c is the frequency of the relevant cavity mode. The spatial dependence of the interaction term is characterized by $\zeta_j = \cos(j\phi)$, with $\phi = \pi\lambda_L/\lambda_c$, which arises because the lattice wavelength $\lambda_L = 813$ nm is incommensurate with the cavity wavelength $\lambda_c = 689$ nm. In contrast to Eq. (1), Eq. (3) becomes non-integrable due to the inhomogeneity in the interaction term. Nevertheless, as shown in Extended Data Fig. 2, Eq. (3) leads to a similar dynamical phase diagram as Eq. (1), if we

- i) Use a generalized superconducting order parameter $\Delta_{\text{BCS}} = \chi \sum_k \zeta_k \langle \hat{S}_k^- \rangle$;
- ii) Interpret the $\pi/2$ -pulse as a pulse along the cavity axis that generates the maximum possible Δ_{BCS} , $\hat{H}_{\text{drive}} = \hbar\Omega \sum_k \zeta_k S_k^y$. It is achieved at $\Omega t = 0.586\pi$;
- iii) Interpret the interaction strength χN as the averaged interaction strength of Eq. (3). It corresponds to replacing χ with $\chi/2$.

We can still measure the generalized order parameter Δ_{BCS} using the field leaking out of the cavity as in the previous section, since with inhomogeneous coupling the transmitted field takes the form $\alpha_{\text{out}}(t) = -\frac{g}{\delta_c} \sqrt{\kappa_m} \sum_k \zeta_k \langle \hat{S}_k^-(t) \rangle \propto \Delta_{\text{BCS}}$. The dynamical phase diagram in Extended Data Fig. 2 is numerically calculated based on unitary evolution under Eq. (3), with a single-particle dispersion ϵ_k sampled from a uniform distribution in the frequency range $[-\delta_s/2 - E_W/2, -\delta_s/2 + E_W/2]$ and $[\delta_s/2 - E_W/2, \delta_s/2 + E_W/2]$. There χN corresponds to the averaged interaction strength of Eq. (3). We identify the dynamical phases based on the long-time average of $|\Delta_{\text{BCS}}|$:

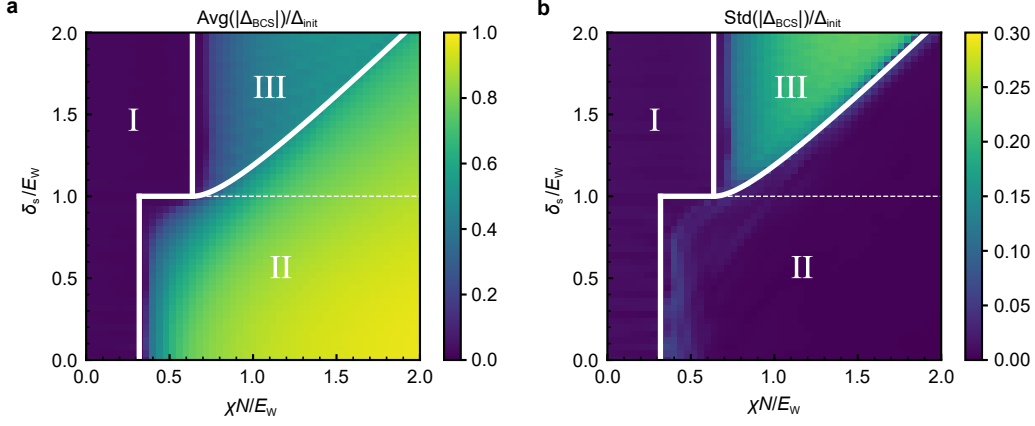
$$\text{Avg}(|\Delta_{\text{BCS}}|) = \lim_{T \rightarrow \infty} \frac{1}{T} \int_0^T |\Delta_{\text{BCS}}(t)| dt, \quad (4)$$

and the long-time oscillation amplitude of $|\Delta_{\text{BCS}}|$. Since the oscillations in $|\Delta_{\text{BCS}}|$ might deviate from a sinusoidal form, it is easier to use the standard deviation as a measure of the oscillation amplitude:

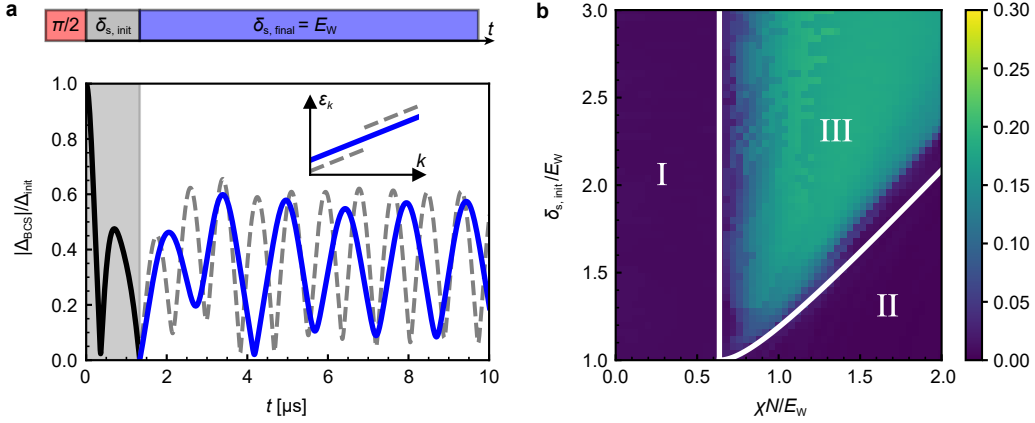
$$\begin{aligned} \text{Std}(|\Delta_{\text{BCS}}|) &= \left[\lim_{T \rightarrow \infty} \frac{1}{T} \int_0^T \left(|\Delta_{\text{BCS}}(t)| - \text{Avg}(|\Delta_{\text{BCS}}|) \right)^2 dt \right]^{1/2}. \end{aligned} \quad (5)$$

In the experiment it is better to use the peak of the Fourier spectrum to reduce noise (see Fig. 3d). The dynamical phases can be characterized by

- Phase I: $\text{Avg}(|\Delta_{\text{BCS}}|) = 0$, $\text{Std}(|\Delta_{\text{BCS}}|) = 0$.
- Phase II: $\text{Avg}(|\Delta_{\text{BCS}}|) > 0$, $\text{Std}(|\Delta_{\text{BCS}}|) = 0$.



Extended Data Fig. 2. Numerical simulation of the dynamical phase diagram based on Eq. (3). We identify the dynamical phases based on a long-time average (a) and the long-time standard deviation (b) of $|\Delta_{\text{BCS}}(t)|$, normalized by its initial value $\Delta_{\text{init}} \equiv |\Delta_{\text{BCS}}(0)|$. The white solid lines mark the corresponding dynamical phase boundaries, analytically derived from Eq. (1), which agree with the numerical results based on Eq. (3). The white dashed lines mark an extra dynamical phase transition that only exists for Eq. (1).



Extended Data Fig. 3. Alternative approach for phase III. a, As described by the timing sequence at the top, we prepare the initial state using a $\pi/2$ pulse, evolve under a bimodal distribution of single-particle energy (see the inset) until $|\Delta_{\text{BCS}}|$ reaches its minimum value, and then quench the system back to a continuous distribution of single-particle energy (see the inset). The theoretical predicted time trace of $|\Delta_{\text{BCS}}|$ with $\chi N/E_W = 1.0$ and $\delta_{s,\text{init}}/E_W = 1.6$ is shown at the bottom. The blue (gray dashed) line shows the phase III dynamics under the continuous (bimodal) distribution. b, Long-time standard deviation of $|\Delta_{\text{BCS}}(t)|$ after quenching to the continuous distribution shown in a. The white lines are dynamical phase boundaries for bimodal distributions (see Extended Data Fig. 2). Nearly all the choices of parameter for phase III using bimodal distributions can lead to phase III behaviors after quenching to the continuous distribution.

- Phase III: $\text{Avg}(|\Delta_{\text{BCS}}|) > 0$, $\text{Std}(|\Delta_{\text{BCS}}|) > 0$.

The dynamical phase boundaries (white solid lines) in Extended Data Fig. 2 are analytically calculated using a Lax analysis applied to Eq. (1), similar to the one discussed in [9], and take the following form:

- Phase I to phase II:

$$\begin{aligned} \frac{\chi N}{E_W} &= \frac{1}{\pi} \quad \text{with} \quad \frac{\delta_s}{E_W} \in [0, 1], \\ \frac{\delta_s}{E_W} &= 1 \quad \text{with} \quad \frac{\chi N}{E_W} \in \left[\frac{1}{\pi}, \frac{2}{\pi} \right]. \end{aligned} \quad (6)$$

- Phase I to phase III:

$$\frac{\chi N}{E_W} = \frac{2}{\pi} \quad \text{with} \quad \frac{\delta_s}{E_W} > 1. \quad (7)$$

- Phase II to phase III:

$$\frac{\delta_s}{E_W} = \csc\left(\frac{E_W}{\chi N}\right) \quad \text{with} \quad \frac{\chi N}{E_W} > \frac{2}{\pi}. \quad (8)$$

The analytical results agree with the numerical simulations for Eq. (3). The only difference is that Eq. (1)

predicts an extra dynamical phase transition marked by the white dashed line. The dynamical phase boundaries shown in Fig. 1c are constructed by the analytical formulas above.

E. Phase III dynamics: the case of a continuous single-particle dispersion

In this manuscript, we generate phase III using a bimodal single-particle dispersion (see Fig. 1b computed assuming ideal conditions and Fig. 3a using actual experimental conditions). Here we show that this experimentally convenient approach generates similar phase III dynamics to the one obtained in the case of a continuous dispersion but with different initial conditions.

This is done by the protocol shown in Extended Data Fig. 3a, which uses a bimodal distribution ($\delta_{s,\text{init}} > E_W$) just to generate a state with minimum $|\Delta_{\text{BCS}}|$. At this point the system's dispersion is restored to be continuous by setting $\delta_{s,\text{final}} = E_W$. This approach more closely resembles the phase III quench discussed in actual BCS superconductors, where phase III is observed by quenching from a state with weak BCS pairing gap $|\Delta_{\text{BCS}}|$ to one with a strong pairing gap [6]. Numerical simulations based on Eq. (3) show that nearly all choices of parameters that lead to phase III using a bimodal distribution also lead to phase III dynamics when quenching to a continuous distribution. The only exception is a small parameter regime close to the boundary between phase III and phase II (see Extended Data Fig. 3b). Note that here we use definitions for Δ_{BCS} , the $\pi/2$ pulse, and χN which correspond to Eq. (3), as explained in the previous section.

F. Numerical simulations

The black dashed lines in Figs. 2, 3, and 4 are computed from unitary evolution under Eq. (3) using a single-particle dispersion ϵ_k , sampled from the experimentally engineered distribution.

The black solid lines in the same figures are obtained by adding dissipative processes and axial motion to Eq. (3). The system dynamics is described by the following master equation for the density matrix $\hat{\rho}$, given by

$$\frac{d\hat{\rho}}{dt} = -\frac{i}{\hbar}[\hat{H}, \hat{\rho}] + \mathcal{L}(\hat{L}_c)[\hat{\rho}] + \sum_k \mathcal{L}(\hat{L}_{s,k})[\hat{\rho}]. \quad (9)$$

The Lindblad superoperator takes the form $\mathcal{L}(\hat{L})[\hat{\rho}] = \hat{L}\hat{\rho}\hat{L}^\dagger - \frac{1}{2}(\hat{L}^\dagger\hat{L}\hat{\rho} + \hat{\rho}\hat{L}^\dagger\hat{L})$. Superradiance through the cavity is described by the jump operator

$$\hat{L}_c = \sqrt{\Gamma} \sum_k \zeta_k \hat{S}_k^-, \quad (10)$$

where $\Gamma = \chi\kappa/\delta_c$. Spontaneous emission from the atomic excited state is described by the jump operator

$$\hat{L}_{s,k} = \sqrt{\gamma} \hat{S}_k^-, \quad (11)$$

where $\gamma/2\pi = 7.5$ kHz is the spontaneous emission rate of 3P_1 states. These are the dominant dissipative processes in our system.

The axial trapping frequency of the lattice is 165 kHz and therefore smaller than the spin-exchange interaction rate χN for most of the experiments. As a consequence, in contrast to the idealized model where atoms are assumed to be frozen, motional processes need to be accounted for, although they are suppressed in the Lamb-Dicke regime. As shown in the Supplemental Online Material, axial motion can lead to a faster damping rate of $|\Delta_{\text{BCS}}|$ oscillations. The predicted dynamical phase boundaries are nevertheless unaffected by the axial motion.

All the numerical simulations are computed using the mean-field approximation, which replaces the operators $\hat{S}_k^{x,y,z}$ by their expectation values $\langle \hat{S}_k^{x,y,z} \rangle$ in the Heisenberg equation of motion. The mean-field treatment of the BCS model is predicted to be exact in the thermodynamic limit due to the infinite-range nature of the interactions [6]. The atom number for numerical simulation is set to 5000 for the ideal conditions and 2000 for actual experimental conditions. We rescale χ to match χN with experimental values.

ACKNOWLEDGMENTS

This material is based upon work supported by the U.S. Department of Energy, Office of Science, National Quantum Information Science Research Centers, Quantum Systems Accelerator. We acknowledge additional funding support from the National Science Foundation under Grant Numbers 1734006 (Physics Frontier Center) and OMA-2016244 (QLCI), NIST, DARPA/ARO W911NF-19-1-0210 and W911NF-16-1-0576, and AFOSR grants FA9550-18-1-0319 and FA9550-19-1-0275. We acknowledge helpful discussions with Victor Gurarie and Adam Kaufman.

Observing Dynamical Phases of a Bardeen-Cooper-Schrieffer Superconductor in a Cavity QED Simulator: Supplemental Materials

S1. EXPERIMENTAL CONTROL OF DYNAMICAL PHASES

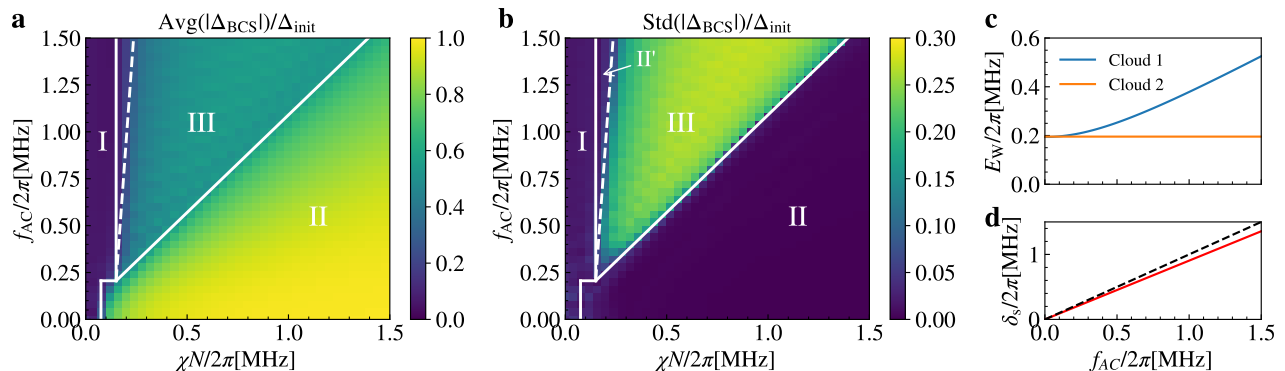


Fig. S1. Experimental control of dynamical phases. **a** and **b**, Dynamical phase diagram for the experiment with two atomic ensembles, in terms of averaged spin exchange interaction strength χN and peak AC Stark shift f_{AC} . The white lines are the estimation of the dynamical phase boundary to guide the eye. The white dashed line marks a small region of phase II' due to the imbalance of E_W for the two atomic ensembles. **c**, E_W as a function of peak AC Stark shift f_{AC} , with AC Stark shift applying to atomic cloud 1. **d**, δ_s as a function of peak AC Stark shift f_{AC} (red line). The dashed line marks the place where $\delta_s = f_{AC}$.

In the experiment that probes the phase I to phase II transition, we use a single atomic ensemble ($\delta_s = 0$) and apply an AC Stark shift beam to generate E_W , as discussed in the Methods. This allows us to use a single-particle transition frequency (ϵ_k) generated from a roughly uniform distribution. So the dynamical phases can be well captured by the Extended Data Fig. 2 with $\delta_s = 0$.

In the other experiments probing the transitions to phase III, we use two atomic ensembles and apply an AC Stark shift beam (peak AC Stark shift f_{AC}) to the first ensemble to generate δ_s . E_W is generated by differential light shifts from the lattice, as discussed in the Methods. In practice, the Gaussian profile of the AC Stark shift beam leads to an increase in E_W for the first atomic ensemble, as well as a reduction of the expected splitting of the two ensembles $\delta_s < f_{AC}$, as shown in Fig. S1c and d. Using the experimental parameters, we get the dynamical phase diagram as depicted in Fig. S1a and b. The imbalance of E_W for the two atomic ensembles can lead to a small region of phase II' marked by the white dashed line. This occurs because the spin exchange interaction is able to lock the ensemble with smaller E_W , while the ensemble with larger E_W remains unlocked. This leads to $|\Delta_{BCS}|$ approaching a small but non-zero constant value. In experiment, due to other dissipative processes and reduced signal-to-noise ratio for small χN , we do not observe a difference between phase I and phase II'. This is the cause of a small discrepancy between theory and experiment in Fig. 4b in the main text in identifying the position of the phase transition.

S2. SHORT-TIME SIGNATURES OF DYNAMICAL PHASES

In this section, we discuss ways to determine the dynamical phases using short-time observables, since the dissipative processes and noise in experiment prevent measuring long-time observables. Phase I can be easily characterized by the fast decay of $|\Delta_{BCS}|$. The phase II to phase III transition can be captured by the dip in the short-time oscillation frequency of $|\Delta_{BCS}|$. Finally we provide an explanation of the frequency dip using an analytical solution of the two-spin BCS model.

A. Phase I: fast decay

In phase I, the single-particle energy term $\sum_k \epsilon_k \hat{S}_k^z$ dominates over the spin exchange interaction. To leading order, one can calculate $|\Delta_{\text{BCS}}|$ in the homogeneous model by dropping the interaction term, which gives

$$\begin{aligned} \frac{|\Delta_{\text{BCS}}|}{\chi N} &\approx \frac{1}{2N} \left| \sum_k e^{-i\epsilon_k t} \right| = \frac{1}{2} \left| \frac{1}{2E_W} \int_{-\delta_s/2 - E_W/2}^{-\delta_s/2 + E_W/2} e^{-ixt} dx + \frac{1}{2E_W} \int_{\delta_s/2 - E_W/2}^{\delta_s/2 + E_W/2} e^{-ixt} dx \right| \\ &= \frac{1}{2} \left| \cos\left(\frac{\delta_s}{2}\right) \right| \cdot \left| \frac{\sin(E_W t/2)}{E_W t/2} \right|. \end{aligned} \quad (\text{S1})$$

The decay profile of $|\Delta_{\text{BCS}}|$ is set by the sinc function with a $1/e$ coherence time $E_W t/2\pi \approx 0.7$. For the inhomogeneous model a similar fast decay time scale of the order of $E_W t/2\pi \sim 1$ can be derived. As shown in Fig. 2b in the main text, we observe fast decay of $|\Delta_{\text{BCS}}|$ within 1 μs in phase I. The decay time scale for the other dynamical phases can be more than 10 times longer.

B. Phase II to phase III transition: frequency dip

In the main text, we discuss a way to understand the phase II to phase III transition by visualizing the two atomic ensembles as two large spins. For the inhomogeneous model, phase II exists in the small δ_s regime, where the two spins lock to each other and form a single large spin through spin-exchange interactions. In this case the many-body gap protection leads to the damped oscillations observed in phase II. Increasing δ_s in phase II leads to the reduction of the many-body gap, and hence to a decrease of the corresponding oscillation frequency. Phase III exists in the large δ_s regime, where the spin locking occurs separately in each ensemble, and the two large spin are instead precessing around each other, with a rate set by the splitting δ_s and the spin-exchange interaction. Increasing δ_s in phase III leads to a speed up of the oscillation frequency. Therefore one expects the existence of a frequency dip separating between phase II and phase III. Indeed as shown in Fig. S2c and d, we find good agreement between the frequency dip and the corresponding dynamical critical point. For small δ_s , the oscillation frequency approaches $2\Delta_\infty \equiv 2 \lim_{t \rightarrow \infty} |\Delta_{\text{BCS}}(t)|$, which agrees with the frequency of the expected Higgs oscillations. For large δ_s , the oscillation frequency approaches δ_s . The reduction of oscillation frequency compared to δ_s indicates many-body effects in phase III.

C. Frequency dip in the two-spin BCS model

Here we use analytical mean field solution of the BCS Hamiltonian with two large spins ($S = N/4$ for each spin) to understand the frequency dip discussed above. The Hamiltonian simplifies to

$$\hat{H}/\hbar = \chi \hat{S}^+ \hat{S}^- + \frac{\delta_s}{2} \hat{S}_1^z - \frac{\delta_s}{2} \hat{S}_2^z, \quad (\text{S2})$$

where $\hat{S}^\pm = \hat{S}_1^\pm + \hat{S}_2^\pm$. The mean field equations of motion for the Hamiltonian above can be written as

$$\begin{aligned} \frac{d}{dt} S_1^x &= 2\chi S^y S_1^z - \frac{\delta_s}{2} S_1^y, & \frac{d}{dt} S_1^y &= -2\chi S^x S_1^z + \frac{\delta_s}{2} S_1^x, & \frac{d}{dt} S_1^z &= -2\chi(S_2^y S_1^x - S_2^x S_1^y), \\ \frac{d}{dt} S_2^x &= 2\chi S^y S_2^z + \frac{\delta_s}{2} S_2^y, & \frac{d}{dt} S_2^y &= -2\chi S^x S_2^z - \frac{\delta_s}{2} S_2^x, & \frac{d}{dt} S_2^z &= -2\chi(S_1^y S_2^x - S_1^x S_2^y). \end{aligned} \quad (\text{S3})$$

The spin components without the hat, represent the expectation value of the corresponding spin operators.

In the following, we focus on the initial state with $S_1^x = S_2^x = N/4$, $S_1^y = S_2^y = S_1^z = S_2^z = 0$. The conserved quantities of the two-spin BCS model are the total magnetization

$$S^z = S_1^z + S_2^z = 0, \quad (\text{S4})$$

total energy

$$E/\hbar = \chi S^+ S^- + \frac{\delta_s}{2} S_1^z - \frac{\delta_s}{2} S_2^z = \chi \left(\frac{N}{2}\right)^2, \quad (\text{S5})$$

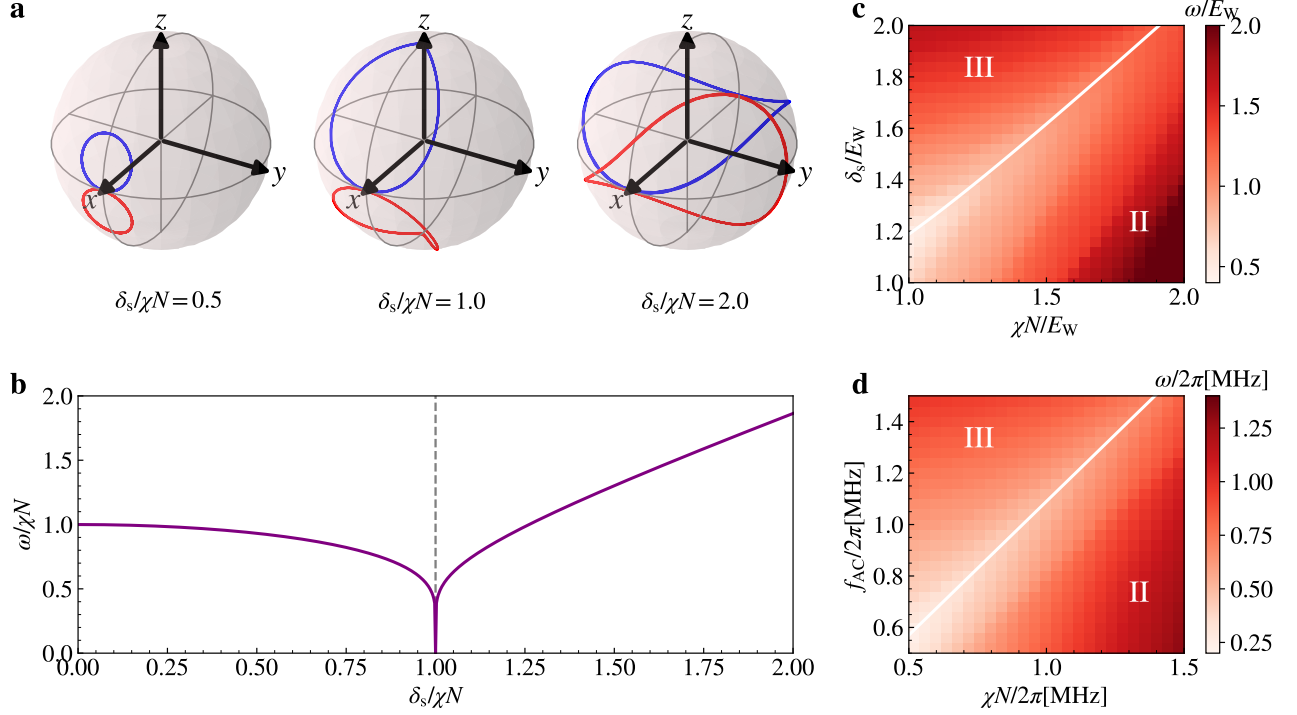


Fig. S2. Frequency dip as a signature of the phase II to phase III transition. **a**, Mean field trajectories of the two large spin model evolving under Eq. (S2). From left to right we set $\delta_s/(\chi N) = 0.5, 1, 2$. **b**, Oscillation frequency of $|\Delta_{\text{BCS}}|$ in the two-spin BCS model Eq. (S2) as a function of $\delta_s/\chi N$. The frequency dip at $\delta_s/\chi N = 1$ marks the dynamical phase transition point. **c**, Short-time frequency ω of the dynamics under inhomogeneous atom-light couplings (see Eq. (3) in the Methods). The white line marks the phase III to phase II transition which is the same as Extended Data Fig. 2 in the Methods. **d**, Short-time frequency ω of the dynamics under experimental control parameters. The white line marks the phase III to phase II transition which is the same as Fig. S1. The frequency dips match the dynamical critical points for both cases.

as well as the spin length of each of the large spins, $(S_1^x)^2 + (S_1^y)^2 + (S_1^z)^2 = (N/4)^2$, $(S_2^x)^2 + (S_2^y)^2 + (S_2^z)^2 = (N/4)^2$. Using these conserved quantities, one can derive from the mean field equations, Eq. (S3), an equation of motion for the BCS order parameter, $\Delta_{\text{BCS}} = \chi S^-$. To simplify the notation, we define $\Delta \equiv |\Delta_{\text{BCS}}|/\chi N$, i.e. $\Delta^2 = S^+ S^-/N^2$. From Eq. (S4) and Eq. (S5), we obtain

$$\frac{d}{dt} \Delta^2 = -\frac{\delta_s}{\chi N^2} \frac{d}{dt} S_1^z = \frac{2\delta_s}{N^2} (S_2^y S_1^x - S_2^x S_1^y), \quad (\text{S6})$$

which leads to

$$\begin{aligned} \frac{d^2}{dt^2} \Delta^2 &= \frac{2\delta_s}{N^2} \left(S_1^x \frac{d}{dt} S_2^y + S_2^y \frac{d}{dt} S_1^x - S_1^y \frac{d}{dt} S_2^x - S_2^x \frac{d}{dt} S_1^y \right) \\ &= 4\delta_s \chi \Delta^2 S_1^z - \frac{2\delta_s^2}{N^2} (S_1^x S_2^x + S_1^y S_2^y). \end{aligned} \quad (\text{S7})$$

Using the following relations which are equivalent to the conserved quantities, $\delta_s S_1^z = -\chi N^2 (\Delta^2 - 1/4)$, $2(S_1^x S_2^x + S_1^y S_2^y) = N^2 \Delta^2 - 2 \times (N/4)^2 + 2(S_1^z)^2$ and plugging then into the time evolution we get

$$\frac{d^2}{dt^2} \Delta^2 = -6(\chi N)^2 (\Delta^2)^2 + \left(2(\chi N)^2 - \delta_s^2 \right) \Delta^2 + \frac{\delta_s^2 - (\chi N)^2}{8}. \quad (\text{S8})$$

The equation above can be further simplified to

$$\frac{1}{2} \left(\frac{d}{dt} \Delta \right)^2 + V(\Delta) = 0, \quad (\text{S9})$$

where

$$V(\Delta) = \frac{1}{2}(\chi N)^2 \left(\Delta^2 - \frac{1}{4} \right) \left(\Delta^2 - \frac{1 - (\delta_s/\chi N)^2}{4} \right), \quad (\text{S10})$$

with an initial condition $\Delta = 1/2$. Eq. (S9) can be understood as a classical particle with position Δ oscillating in the potential $V(\Delta)$. For $\delta_s < \chi N$, we find Δ oscillating between $\Delta_{\max} = 1/2$ and $\Delta_{\min} = \sqrt{1 - (\delta_s/\chi N)^2}/2$. This is equivalent to phase II in the cases of many spins with inhomogeneous atom-light couplings, because all the oscillations damp in the large χN limit. For $\delta_s > \chi N$, we find Δ oscillating between $\Delta_{\max} = 1/2$ and $\Delta_{\min} = 0$, since the definition of Δ requires $\Delta \geq 0$. This is equivalent to phase III in the cases of many spins, because the phase connects to single-particle oscillations in the large δ_s limit. Therefore, a dynamical phase transition occurs at $\delta_s/\chi N = 1$, which is equivalent to the phase II to phase III transition in the cases of many spins.

The analytical solution of Eq. (S9) can be written in terms of Jacobian elliptic functions dn and cn ,

$$\Delta(t) = \begin{cases} \frac{1}{2} \text{dn} \left(\frac{1}{2} \chi N t \left| (\delta_s/\chi N)^2 \right. \right) & \text{if } \delta_s < \chi N \\ \frac{1}{2} \left| \text{cn} \left(\frac{1}{2} \delta_s t \left| (\chi N/\delta_s)^2 \right. \right) \right| & \text{if } \delta_s > \chi N \end{cases}. \quad (\text{S11})$$

The frequency of $\Delta(t)$ can be written in terms of the complete elliptic integral of the first kind $K(k^2)$,

$$\frac{\omega}{\chi N} = \begin{cases} \frac{\pi}{2K \left((\delta_s/\chi N)^2 \right)} & \text{if } \delta_s < \chi N \\ \frac{\delta_s}{\chi N} \frac{\pi}{2K \left((\chi N/\delta_s)^2 \right)} & \text{if } \delta_s > \chi N \end{cases}. \quad (\text{S12})$$

The mean-field trajectories on the Bloch sphere are shown in Fig. **S2a**, and the oscillation frequency Eq. (S12) are shown in Fig. **S2b**. The dynamical phase transition can also be understood from the mean field trajectories. For $\delta_s < \chi N$, the two large spins are locking to each other and oscillating near x axis of the Bloch sphere. For $\delta_s > \chi N$, the two large spins are unlocked and precessing around the whole Bloch sphere. Near the dynamical critical point, the mean field trajectories are close to the north pole or south pole of the Bloch sphere, which leads to a slow down of the oscillations because they approach stable fixed points of the Hamiltonian.

S3. AXIAL MOTION

In this section, we elaborate on how to take account of the axial motion in our system. Similar discussions can be found in Ref. [32]. We start from the one-dimensional Hamiltonian of our cavity QED system with two internal atomic levels ($|\uparrow\rangle$ and $|\downarrow\rangle$),

$$\begin{aligned} \hat{H} = & \sum_{\sigma=\{\uparrow,\downarrow\}} \int dx \hat{\psi}_{\sigma}^{\dagger}(x) \left[\frac{\hat{p}^2}{2M} + V_0 \sin^2(k_L x) \right] \hat{\psi}_{\sigma}(x) + \int dx \hat{\psi}_{\uparrow}^{\dagger}(x) \left[\hbar\omega_0 + U_{ac}(x) \right] \hat{\psi}_{\uparrow}(x) \\ & + \hbar g_c \int dx \cos(k_c x) \left[\hat{\psi}_{\uparrow}^{\dagger}(x) \hat{\psi}_{\downarrow}(x) \hat{a} + \hat{a}^{\dagger} \hat{\psi}_{\downarrow}^{\dagger}(x) \hat{\psi}_{\uparrow}(x) \right] + \hbar\omega_c \hat{a}^{\dagger} \hat{a}, \end{aligned} \quad (\text{S13})$$

where $k_L = 2\pi/\lambda_L$ is the wave number of the lattice beams ($\lambda_L = 813\text{nm}$), k_c is the wave number of the cavity mode ($\lambda_c = 689\text{nm}$), ω_0 is the atomic transition frequency between $|\uparrow\rangle$ and $|\downarrow\rangle$ states, $U_{ac}(x)$ is the AC Stark shift applied to the atoms (including the differential light shift from the lattice beams and the transverse AC Stark shift beam), ω_c is the frequency of cavity resonance.

Since the atoms are trapped in an optical lattice with lattice depth of the order of $10^3 E_R$, we can approximate each lattice site as an harmonic trap with axial trapping frequency $\hbar\omega_T = \sqrt{4V_0 E_R}$, where $E_R = \hbar^2 k_L^2 / 2M$ is the lattice recoil energy. We also ignore tunneling processes between lattice sites. In this case, one can expand the atomic field operator in terms of lattice site index j and harmonic oscillator levels n ,

$$\hat{\psi}_{\sigma}(x) = \sum_{jn} \hat{c}_{jn,\sigma} \phi_n(x - ja_L), \quad (\text{S14})$$

where $a_L = \lambda_L/2$ is the lattice spacing, ϕ_n is the harmonic oscillator wave function for mode n ,

$$\phi_n(x) = \frac{1}{\sqrt{2^n n!}} \left(\frac{M\omega_T}{\pi\hbar} \right)^{1/4} e^{-M\omega_T x^2/2\hbar} H_n \left(\sqrt{\frac{M\omega_T}{\hbar}} x \right), \quad (\text{S15})$$

with $H_n(x)$ Hermite polynomials. Plugging this expansion into the Hamiltonian and transform to the rotating frame of the atoms, we obtain

$$\hat{H}/\hbar = \sum_{jn\sigma} n\omega_T \hat{c}_{jn,\sigma}^\dagger \hat{c}_{jn,\sigma} + \sum_{jn} \epsilon_{jn} \hat{c}_{jn,\uparrow}^\dagger \hat{c}_{jn,\uparrow} + g_c \sum_{jnm} \zeta_j^{nm} (\hat{c}_{jn,\uparrow}^\dagger \hat{c}_{jm,\downarrow} \hat{a} + \hat{a}^\dagger \hat{c}_{jm,\downarrow}^\dagger \hat{c}_{jn,\uparrow}) + \delta_c \hat{a}^\dagger \hat{a}, \quad (\text{S16})$$

where $\delta_c = \omega_c - \omega_a$. For simplicity, we assume $U_{ac}(x)$ is either small or slowly varying in space and thus does not change the trap geometry. This term gives rise to inhomogeneous transition frequency $\epsilon_{jn} = \int dx U_{ac}(x) [\phi_n(x - ja_L)]^2/\hbar$. We calculate ζ_j^{nm} in the following way:

$$\begin{aligned} \zeta_j^{nm} &= \int dx \cos(k_c x) \phi_n(x - ja_L) \phi_m(x - ja_L) = \int dx \cos(k_c x + k_c ja_L) \phi_n(x) \phi_m(x) \\ &= \cos(j\varphi) \int dx \cos(k_c x) \phi_n(x) \phi_m(x) - \sin(j\varphi) \int dx \sin(k_c x) \phi_n(x) \phi_m(x) \\ &= \cos(j\varphi) \text{Re} \left[(i\eta)^s e^{-\eta^2/2} \sqrt{\frac{n_{<}}{n_{>!}}} L_{n_{<}}^s(\eta^2) \right] - \sin(j\varphi) \text{Im} \left[(i\eta)^s e^{-\eta^2/2} \sqrt{\frac{n_{<}}{n_{>!}}} L_{n_{<}}^s(\eta^2) \right]. \end{aligned} \quad (\text{S17})$$

where $\varphi = \pi k_L/k_c$, $s = |n - m|$, $n_{<} = \min(n, m)$, $n_{>} = \max(n, m)$, $L_n^\alpha(x)$ are generalized Laguerre polynomials, and $\eta = k_c \sqrt{\hbar/2M\omega_T}$ is the Lamb-Dicke parameter. In our case $\omega_T/2\pi = 165\text{kHz}$, we have $\eta = 0.17$, which means ζ_j^{nm} become negligible for $|n - m| > 1$. It's convenient to rewrite the Hamiltonian in terms of operators $\hat{S}_{n\sigma, m\sigma'}^j = \hat{c}_{jn,\sigma}^\dagger \hat{c}_{jm,\sigma'}$ and obtain:

$$\hat{H}/\hbar = \sum_{jn\sigma} n\omega_T \hat{S}_{n\sigma, n\sigma}^j + \sum_{jn} \epsilon_{jn} \hat{S}_{n\uparrow, n\uparrow}^j + g_c \sum_{jnm} \zeta_j^{nm} (\hat{S}_{n\uparrow, m\downarrow}^j \hat{a} + \hat{a}^\dagger \hat{S}_{m\downarrow, n\uparrow}^j) + \delta_c \hat{a}^\dagger \hat{a}. \quad (\text{S18})$$

In addition to the Hamiltonian dynamics, we also consider the dissipation processes such as cavity loss with a rate $\kappa/2\pi = 153\text{kHz}$, and spontaneous emission with a rate $\gamma/2\pi = 7.5\text{kHz}$, so the dynamics of this system can be described by the following Lindblad master equation,

$$\frac{d}{dt} \hat{\rho} = -\frac{i}{\hbar} [\hat{H}, \hat{\rho}] + \left[\hat{L}_{\text{cav}} \hat{\rho} \hat{L}_{\text{cav}}^\dagger - \frac{1}{2} \{ \hat{L}_{\text{cav}}^\dagger \hat{L}_{\text{cav}}, \hat{\rho} \} \right] + \sum_{jn} \left[\hat{L}_{j,n} \hat{\rho} \hat{L}_{j,n}^\dagger - \frac{1}{2} \{ \hat{L}_{j,n}^\dagger \hat{L}_{j,n}, \hat{\rho} \} \right], \quad (\text{S19})$$

where jump operator for cavity loss is given by $\hat{L}_{\text{cav}} = \sqrt{\kappa} \hat{a}$, and the single-particle jump operators for spontaneous emission are given by $\hat{L}_{j,n} = \sqrt{\gamma} \hat{S}_{n\downarrow, n\uparrow}^j$. Here, we assume the spontaneous emission is in the Lamb-Dicke regime.

In experiment, δ_c is the largest frequency scale ($\delta_c \gg g_c \sqrt{N}, \kappa$), so we can adiabatically eliminate the cavity photons [48], and obtain an effective atom-only master equation,

$$\frac{d}{dt} \hat{\rho} = -\frac{i}{\hbar} [\hat{H}_{\text{eff}}, \hat{\rho}] + \left[\hat{L}_{\text{col}} \hat{\rho} \hat{L}_{\text{col}}^\dagger - \frac{1}{2} \{ \hat{L}_{\text{col}}^\dagger \hat{L}_{\text{col}}, \hat{\rho} \} \right] + \sum_{jn} \left[\hat{L}_{j,n} \hat{\rho} \hat{L}_{j,n}^\dagger - \frac{1}{2} \{ \hat{L}_{j,n}^\dagger \hat{L}_{j,n}, \hat{\rho} \} \right], \quad (\text{S20})$$

where the effective Hamiltonian is given by

$$\hat{H}_{\text{eff}}/\hbar = \sum_{jn\sigma} n\omega_T \hat{S}_{n\sigma, n\sigma}^j + \sum_{jn} \epsilon_{jn} \hat{S}_{n\uparrow, n\uparrow}^j + \chi \sum_{jnm} \sum_{kpq} \zeta_j^{nm} \zeta_k^{pq} \hat{S}_{n\uparrow, m\downarrow}^j \hat{S}_{p\downarrow, q\uparrow}^k, \quad (\text{S21})$$

and effective collective jump operator generating superradiant decay is given by

$$\hat{L}_{\text{col}} = \sqrt{\Gamma} \sum_{jnm} \zeta_j^{nm} \hat{S}_{m\downarrow, n\uparrow}^j, \quad (\text{S22})$$

with $\chi = -g_c^2 \delta_c / (\delta_c^2 + \kappa^2/4)$ and $\Gamma = g_c^2 \kappa / (\delta_c^2 + \kappa^2/4)$. The equivalent superconducting order parameter takes the following form,

$$\Delta_{\text{BCS}} = \chi \sum_{kpq} \zeta_k^{pq} \langle \hat{S}_{p\downarrow, q\uparrow}^k \rangle. \quad (\text{S23})$$

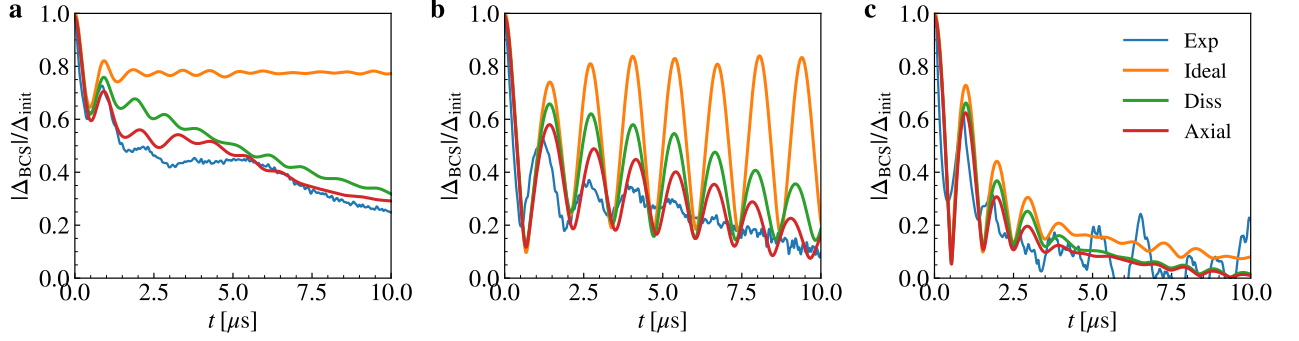


Fig. S3. Understanding experimental results with axial motion effects. **a** Example phase II traces with $\chi N/2\pi = 1.29\text{MHz}$, $f_{AC}/2\pi = 1.1\text{MHz}$. **b** Example phase III traces with $\chi N/2\pi = 0.79\text{MHz}$, $f_{AC}/2\pi = 1.1\text{MHz}$. **c** Example phase I traces with $\chi N/2\pi = 0.15\text{MHz}$, $f_{AC}/2\pi = 1.1\text{MHz}$. The blue points are experimental data, the orange lines are numerical simulation for ideal conditions (see Eq. (3) in the Methods), the green lines are adding dissipative processes to ideal conditions, and the red lines are adding dissipative processes and axial motion effects to ideal conditions.

One can recover the inhomogeneous model discussed in the previous section by removing the axial harmonic oscillator level labels.

Similarly, the Hamiltonian for initial state preparation takes the following form,

$$\hat{H}_{\text{drive}}/\hbar = \sum_{jn\sigma} n\omega_T \hat{S}_{n\sigma, n\sigma}^j + \frac{1}{2} \sum_{jnm} \zeta_j^{nm} (\Omega \hat{S}_{n\uparrow, m\downarrow}^j + \Omega^* \hat{S}_{m\downarrow, n\uparrow}^j). \quad (\text{S24})$$

In numerical simulations, we perform a mean-field approximation, which replaces the operators $\hat{S}_{p\sigma, q\sigma'}^j$ by their expectation values $\langle \hat{S}_{p\sigma, q\sigma'}^j \rangle$ in the Heisenberg equation of motion. We perform a random sampling of the axial harmonic oscillator mode n for each atom based on thermal distribution of $15 \mu\text{K}$, and only include the modes n and $n \pm 1$ into our calculation due to the Lamb-Dicke parameter. The atom number for numerical simulation is set to 2000, and we rescale χ to keep χN to be the experimental value. We also empirically take into account two additional dissipation processes to quantitatively capture the behavior of $|\Delta_{\text{BCS}}|$ at longer time scales: 1) single-particle decoherence between electronic states, described by the jump operators $\hat{L}_{j, \sigma}^{\text{el}} = \sqrt{\gamma_{\text{el}}} \sum_n \hat{S}_{n\sigma, n\sigma}^j$ with $\gamma_{\text{el}}/2\pi < 1\text{kHz}$ for Fig. 2 starting from $t = 0\mu\text{s}$, $\gamma_{\text{el}}/2\pi = 0.0036(f_{AC}/2\pi) + 0.004\text{kHz}$ for Fig. 3 and Fig. 4 in the main text. 2) single-particle decoherence between motional states, described by the jump operators $\hat{L}_{j, n}^{\text{mo}} = \sqrt{\gamma_{\text{mo}}} \sum_{\sigma} \hat{S}_{n\sigma, n\sigma}^j$ with $\gamma_{\text{mo}}/2\pi = 15\text{kHz}$.

Some example traces including axial motion effects are depicted in Fig. S3. Generally speaking, the predicted dynamical phases are nevertheless unaffected by the axial motion, while it allows us to capture the details of $|\Delta_{\text{BCS}}|$ evolution. As shown in Fig. S3a, for phase II dynamics, including axial motion effects allows us to capture the faster damping rate of the Higgs oscillations, as well as a slow oscillation in $|\Delta_{\text{BCS}}|$ at the axial trapping frequency. As shown in Fig. S3b, for phase III dynamics, including axial motion effects allows us to capture the faster damping rate of the oscillations in $|\Delta_{\text{BCS}}|$, although the damping rate is still faster than the theory predictions. As shown in Fig. S3c, for phase I dynamics, all the theory simulations are similar to the simulation for ideal conditions, which indicates the axial motion is not playing a significant role in this case.